

3D template-based *Fermi*-LAT constraints on axion-like particles¹

Francesca Calore,^{1,*} Pierluca Carenza,^{2,3,4,†} Christopher Eckner,^{1,‡} Tobias Fischer,^{5,§} Maurizio Giannotti,^{6,¶}
Joerg Jaeckel,^{7,**} Kei Kotake,⁸ Takami Kuroda,⁹ Alessandro Mirizzi,^{3,4,††} and Francesco Sivo^{3,‡‡}

¹*Univ. Grenoble Alpes, USMB, CNRS, LAPTh, F-74000 Annecy, France*

²*The Oskar Klein Centre, Department of Physics,
Stockholm University, Stockholm 106 91, Sweden*

³*Dipartimento Interateneo di Fisica “Michelangelo Merlin”, Via Amendola 173, 70126 Bari, Italy.*

⁴*Istituto Nazionale di Fisica Nucleare - Sezione di Bari, Via Orabona 4, 70126 Bari, Italy.*

⁵*Institute of Theoretical Physics, University of Wrocław, 50-204 Wrocław, Poland*

⁶*Physical Sciences, Barry University, 11300 NE 2nd Ave., Miami Shores, FL 33161, USA*

⁷*Institut für theoretische Physik, Universität Heidelberg, Philosophenweg 16, 69120 Heidelberg, Germany*

⁸*Faculty of Science, Department of Applied Physics & Research Institute of Stellar Explosive Phenomena,
Fukuoka University, Fukuoka, Jonan 8-19-1, 814-0180, Japan*

⁹*Max-Planck-Institut für Gravitationsphysik, Am Mühlenberg 1, D-14476 Potsdam-Golm, Germany*
(Dated: July 5, 2022)

Axion-like particles (ALPs) may be abundantly produced in core-collapse (CC) supernovae (SNe), hence the cumulative signal from all past SN events would contain an ALP component and create a diffuse flux peaked at energies of about 50 MeV. We update the calculation of this flux by including a set of CC SN models with different progenitor masses following the expected mass distribution. Additionally, we include the effects of failed CC SNe, which yield the formation of black holes instead of explosions. Relying on the coupling strength of ALPs to photons and the related Primakoff process, the diffuse SN ALP flux is converted into a diffuse gamma-ray flux while traversing the magnetic field of the Milky Way. The spatial morphology of this signal is expected to follow the shape of the Galactic magnetic field lines. We make use of this via a template-based analysis that utilizes 12 years of *Fermi*-LAT data in the energy range from 50 MeV to 500 GeV. This strategy yields an improvement of roughly a factor of two for the upper limit on the ALP-photon coupling constant $g_{a\gamma}$ compared to a previous analysis that accounted only for the spectral shape of the signal. While the improved SN modeling leads to a less energetic flux that is harder to detect, the combined effect is still an improvement of the limit and in particular its statistical reliability. We also show that our results are robust against variations in the modeling of high-latitude Galactic diffuse emission and systematic uncertainties of the LAT.

I. INTRODUCTION

Observing a supernova (SN) provides unique opportunities for fundamental physics. In particular, they are ideally suited to probe feebly interacting particles (cf. [2] for a recent review) with masses up to the ~ 100 MeV range. Indeed, large numbers of such particles can be emitted in SN events [3]. An important and theoretically interesting instance of this are axions and axion-like particles (ALPs) [4, 5]. Indeed, SN 1987A has significantly strengthened astrophysical axion bounds in a region of the yet-incompletely known ALP parameter space, complementary to the one probed by the Sun and the globular

clusters [4, 6–9]. In the minimal scenario in which ALPs are coupled only with photons, the main channel for their emissivity in the SN core is the Primakoff process, leading to an ALP flux peaked at energies of about 50 MeV. Conversion of these ALPs into gamma rays in the Milky Way magnetic field can lead to an observable gamma-ray burst in coincidence with the SN explosion [6, 7]. At the time of the SN 1987A, the Gamma-Ray Spectrometer (GRS) on the Solar Maximum Mission (SMM) had the SN in its field of view and observed no gamma-ray signal at the time of the explosion, this allowed to constrain the photon-ALP coupling early on [6, 7]. In a more refined, recent analysis, this upper limit is stated as $g_{a\gamma} \lesssim 5.3 \times 10^{-12} \text{ GeV}^{-1}$ for $m_a < 4 \times 10^{-10} \text{ eV}$ [10]. A future Galactic SN explosion in the field of view of the Large Area Telescope (LAT) aboard the *Fermi* satellite would allow us to constrain $g_{a\gamma} \lesssim 2.0 \times 10^{-13} \text{ GeV}^{-1}$ for $m_a < 10^{-9} \text{ eV}$ [11]. Furthermore, a search for gamma-ray bursts from extragalactic SNe with *Fermi*-LAT has yielded the limit $g_{a\gamma} \lesssim 2.6 \times 10^{-11} \text{ GeV}^{-1}$ for $m_a < 3 \times 10^{-10} \text{ eV}$ [12] (see also [13, 14]).

While single SN explosions are rare and must fall into the detector field of view to be observed, there exists a guaranteed contribution to the gamma-ray diffuse flux which originates from ALPs emitted by all past SNe in

¹ Parts of this work have already been shown at ICRC 2021 and a short preview has appeared in the associated proceedings [1].

* calore@lapth.cnrs.fr

† pierluca.carenza@fysik.su.se

‡ eckner@lapth.cnrs.fr

§ tobias.fischer@uwr.edu.pl

¶ mgiannotti@barry.edu

** jjaeckel@thphys.uni-heidelberg.de

†† alessandro.mirizzi@ba.infn.it

‡‡ f.sivo1@studenti.uniba.it

the Universe [15]. This Diffuse SN ALP Background (DSNALPB), despite being fainter than the Galactic one, is within the reach of the *Fermi*-LAT experiment. In [16] some of us used published *Fermi*-LAT observations of the gamma-ray isotropic diffuse background to set a bound $g_{a\gamma} \lesssim 5.0 \times 10^{-11} \text{ GeV}^{-1}$ for $m_a < 10^{-11} \text{ eV}$. We note that this analysis does not completely acknowledge the technicalities behind the derivation of the isotropic gamma-ray background, which may impact the reliability of the stated upper bound on $g_{a\gamma}$. This component of the gamma-ray sky is obtained in connection with a particular model of the diffuse gamma-ray flux from the Milky Way and evaluated in a particular region of interest. Both the dependence on the diffuse model and the dependence on the selected sky region introduce unknowns in the upper bound estimate that cannot be cast into an uncertainty on the derived value because it is not known if the initial choices made by the *Fermi*-LAT collaboration create artificially strong or weak limits. Hence, we deem it warranted to put the analysis of the DSNALPB on solid statistical foundations by creating a complete *Fermi*-LAT data analysis pipeline which takes into account all the experience that has been gained over the long run of the LAT.

In the present work, we improve upon the previous analysis presented in [16] in two ways. First, we present a more refined model of the SNe ALPs flux. It is indeed well known that the production of ALPs in a SN event depends on the progenitor mass. In [16], however, it was assumed that all past SNe are represented by a $18 M_\odot$ progenitor model. Here, instead, we consider different CC SN models with masses ranging between 8.8 and $70 M_\odot$, accounting also for the contribution due to failed² core-collapse (CC) SN explosions. This allows us to determine with better accuracy a possible range of variability of the DSNALPB, and, in turn, of the expected gamma-ray flux. Secondly, we try to exploit the full potential of *Fermi*-LAT data in searching for this type of signal, by including information on the expected spatial structure of the signal in the gamma-ray data analysis. Ref. [16] indeed set limits on ALPs solely making use of the spectral energy distribution of the data. On other hand, template-based analyses – see e.g. [17] for an early application in the context of EGRET data or a more recent example of an analysis of *Fermi*-LAT data [18] that led to the discovery of the so-called *Fermi Bubbles* – exploit both spectral and spatial properties of gamma-ray data to constrain physics models. This gamma-ray fitting technique has proven to be particularly successful in testing the hypothesis of weakly interacting massive particles shining in gamma rays at GeV - TeV energies (see, for instance, [19–23]). However, to our knowledge, it

was never applied to the search of an ALPs signal, albeit it presents specific spatial features, as we discuss below. We therefore perform a template-based analysis to constrain the ALP parameter space via the spatial structure of the DSNALPB induced diffuse gamma-ray flux using 12 years of *Fermi*-LAT data in the energy range from 50 MeV to 500 GeV.

In Sec. II, we illustrate the CC SN models based on state-of-the-art hydrodynamical simulations. In Sec. III, we present our updated calculation of the ALPs production flux in SNe and induced gamma-ray flux from the DSNALPB. In Sec. IV, we sketch the analysis framework: data selection and preparation, and template fitting method of *Fermi*-LAT data. We discuss our results in Sec. V. We discuss model systematic uncertainties and their impact on the ALPs upper limits in Sec. VI, and conclude in Sec. VII.

II. CORE-COLLAPSE SUPERNOVA MODELS

In order to provide reliable constraints on the DSNALPB, it is essential to cover a representative, wide range of SN models, which are based on state-of-the-art simulations. The present work discusses SN simulations which are based on general relativistic neutrino radiation hydrodynamics featuring three-flavor neutrino transport, both in spherical symmetry [24–27] with accurate Boltzmann neutrino transport, and in axial symmetry with a multi-energy neutrino transport method [28]. These simulations implement a complete set of weak interactions [29], and a multi-purpose microscopic nuclear matter equation of state (EOS) [30–34].

In what follows, we distinguish successful core-collapse SN explosions of different types of progenitors. We consider the low-mass oxygen-neon-magnesium core progenitor with zero-age main sequence (ZAMS) mass of $8.8 M_\odot$ [35]. They belong to the class of electron-capture SN [36], which yield neutrino-driven SN explosions even in spherical symmetry. The SN simulations discussed here were reported in Ref. [37], based on the nuclear EOS of Ref. [31]. The simulations include all SN phases, i.e. stellar core collapse, core bounce³ with the formation of the bounce shock, the subsequent SN post-bounce mass accretion phase including the explosion onset with the revival of the stalled bounce shock and finally the long-term deleptonization phase of the compact hot and dense central remnant proto-neutron star (PNS). The latter SN phase is of particular importance for the emission of axions. The remnant of this electron-capture SN explosion is a low-mass neutron star with a baryon mass of about $1.37 M_\odot$. The corresponding PNS deleptonization features a nearly constant central density of

² In the supernova models considered here, “failed” supernova is defined by a model with BH formation or without a shock revival during the numerical simulation. We will see the effect this has on the ALP production momentarily.

³ We define the point in time of the core bounce when the maximum central density is reached at the end of the stellar core collapse, which coincides with the time of shock breakout.

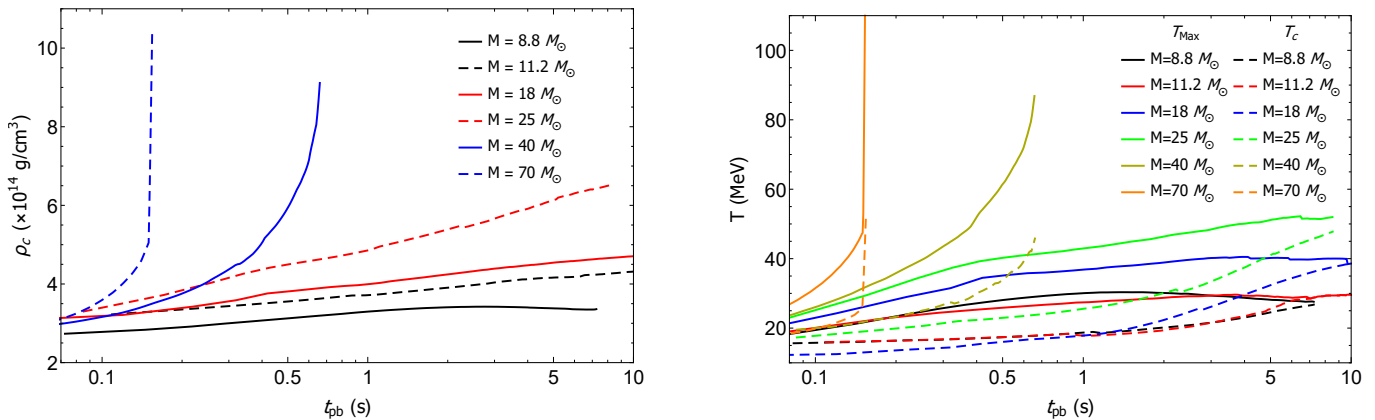


FIG. 1. PNS evolution during the deleptonization phase for the SN explosion models launched from different progenitors with ZAMS masses of 8.8, 11.2, 18.0 and 25 M_{\odot} . *Left panel:* central density, ρ_{centre} . *Right panel:* central and maximum temperatures, T_{centre} (solid lines) and T_{Max} (dashed lines).

$\rho_{\text{central}} \simeq 3.5 \times 10^{14} \text{ g cm}^{-3}$ as well as central temperature decreasing from $T_{\text{Max}} \simeq 30 \text{ MeV}$ to 25 MeV during the PNS deleptonization up to about 7.5 s post bounce, as illustrated in Fig. 1. In addition to the decreasing, central temperature, we show the maximum temperature evolution in Fig. 1, which rises moderately from $T_{\text{core}} \simeq 20 \text{ MeV}$ to about 25 MeV.

As an example of a low-mass iron-core progenitor we consider the example with ZAMS mass of 11.2 M_{\odot} from the stellar evolution series of Ref. [38]. In contrast to electron-capture SN, which are characterized by a short post-bounce mass accretion period on the order of only few tenths of a second before the onset of the explosion, more massive iron-core progenitors suffer from extended post-bounce mass accretion periods, which fail to yield neutrino-driven explosions in self-consistent spherically symmetric simulations. Nevertheless, in order to obtain explosions, the neutrino heating and cooling rates have been enhanced artificially in Ref. [37], which lead to the successful revival of the stalled bounce shock. It results in the SN explosion onset⁴ about 300 ms after core bounce, for this progenitor star of 11.2 M_{\odot} . The subsequent evolution of the central density of $\rho_{\text{centre}} \simeq 4 \times 10^{14} \text{ g cm}^{-3}$ as well as the central and maximum temperatures is illustrated in Fig. 1. The latter differ only marginally from those of the 8.8 M_{\odot} model.

Two more massive iron-core progenitors are included here, with ZAMS masses of 18.0 M_{\odot} and 25 M_{\odot} , which are evolved in a similar fashion as the 11.2 M_{\odot} model leading to neutrino-driven SN explosions on the order of several hundreds of milliseconds after core bounce. However, the remnant PNSs are more massive and hence feature a higher central density as well as higher central and maximum temperatures than the 8.8 and 11.2 M_{\odot}

models (see Fig. 1). In particular the 25 M_{\odot} simulation reaches maximum temperatures at the PNS interior which reach as high as 50 MeV during the PNS deleptonization phase. This aspect is important for the axion emission since the axion emissivity has a strong temperature dependence.

In addition to the successful CC SN explosion models, we consider two examples with ZAMS masses of 40 and 70 M_{\odot} belonging to the failed CC SN branch which yield the formation of black holes instead [39–42]. In such case the mass accretion onto the bounce shock, in combination with the failed shock revival, leads to the continuous growth of the enclosed mass of the PNS until it exceeds the maximum mass given by the nuclear EOS, on a timescale of several hundreds of milliseconds up to one second post bounce. If no phase transition is considered [43, 44], the PNS collapses eventually and a black hole forms. The data for the SN simulation of the 40 M_{\odot} progenitor discussed in the following are taken from Ref. [41] based on the nuclear EOS of Ref. [30]. It results in black hole formation at about 450 ms post bounce with an enclosed PNS mass of about 2.5 M_{\odot} . The most massive progenitor model considered of 70 M_{\odot} , belongs to the class of zero-metallicity stars [45] for which a black hole forms within a few hundred milliseconds after core bounce [28, 46, 47]. This model has been evolved in axially symmetric simulations. Although the original SN simulation [28] takes into account the effect of strong phase transition from nuclear matter to the quark-gluon plasma at high baryon density, the central quark core immediately collapses into a BH within $\sim 1 \text{ ms}$ after its formation. Therefore its influence on ALPs emission is expected to be minor. Furthermore, as the central high temperature region is swallowed by the BH, most of the ALPs emission is expected to cease abruptly once the BH formation occurs, as indicated by ending the lines in Fig. 1. The corresponding baryonic PNS mass at the onset of the PNS collapse is estimated to be $\sim 2.6 M_{\odot}$. In comparison to the other SN explosion

⁴ In all these SN simulations, the onset of the explosions is defined when the expanding shock wave reaches a radius of about 1000 km.

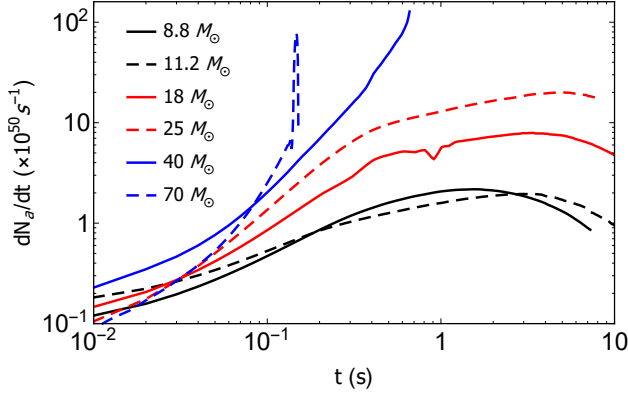


FIG. 2. Time evolution of the SN ALP number flux for different SN mass progenitors. We assume $g_{a\gamma} = 10^{-11} \text{ GeV}^{-1}$ and $m_a \ll 10^{-11} \text{ eV}$.

models, with ZAMS masses of $8.8 - 25 M_\odot$, the failed SN branch yields significantly higher central densities as well as core temperatures. The latter reaches shortly before black hole formation up to $\rho_{\text{centre}} \geq 10^{15} \text{ g cm}^{-3}$ and $T_{\text{Max}} \geq 100 \text{ MeV}$.

Having a set of characteristic supernovae, we will then do a simple interpolation between them, as will be described below.

III. DSNALPB AND GAMMA-RAY FLUX

A. ALPs emission from SNe

We consider a minimal scenario in which ALPs have only a two-photon coupling, characterized by the Lagrangian [48]

$$\mathcal{L}_{a\gamma} = -\frac{1}{4} g_{a\gamma} F_{\mu\nu} \tilde{F}^{\mu\nu} a = g_{a\gamma} \mathbf{E} \cdot \mathbf{B} a. \quad (1)$$

Through this interactions ALPs may be produced in stellar plasma primarily via the Primakoff process [49]. In such a process thermal photons are converted into ALPs in the electrostatic field of ions, electrons and protons. We calculate the ALP production rate (per volume) in a SN core via Primakoff process closely following [10], which finds

$$\frac{d\dot{n}_a}{dE} = \frac{g_{a\gamma}^2 \xi^2 T^3 E^2}{8\pi^3 (e^{E/T} - 1)} \left[\left(1 + \frac{\xi^2 T^2}{E^2} \right) \ln(1 + E^2/\xi^2 T^2) - 1 \right]. \quad (2)$$

Here, E is the photon energy, T the temperature and $\xi^2 = \kappa^2/4T^2$ with κ the inverse Debye screening length, describing the finite range of the electric field surrounding charged particles in the plasma. The total ALP production rate per unit energy is obtained integrating Eq. (2) over the SN volume.

TABLE I. Fitting parameters for the SN ALP production time evolution, Eq. (3), from the Primakoff process for different core-collapse SN estimated for $g_{a\gamma} = 10^{-11} \text{ GeV}^{-1}$ and $m_a \ll 10^{-11} \text{ eV}$.

SN progenitor	$a [\times 10^{50} \text{ s}^{-1}]$	b	$c [\text{s}^{-1}]$
$8.8 M_\odot$	2.75	0.573	0.33
$11.2 M_\odot$	1.95	0.528	0.20
$18 M_\odot$	6.79	0.560	0.16
$25 M_\odot$	11.43	0.609	0.13

TABLE II. Fitting parameters for the SN ALP spectrum, Eq. (4), from the Primakoff process for different SN progenitors estimated for $g_{a\gamma} = 10^{-11} \text{ GeV}^{-1}$ and $m_a \ll 10^{-11} \text{ eV}$.

SN progenitor	$C [\times 10^{50} \text{ MeV}^{-1}]$	$E_0 [\text{MeV}]$	β
$8.8 M_\odot$	2.77	90.80	2.58
$11.2 M_\odot$	4.98	93.39	2.79
$18 M_\odot$	16.0	120.2	2.42
$25 M_\odot$	19.0	147.6	2.25
$40 M_\odot$	1.43	174.4	1.81
$70 M_\odot$	0.18	109.8	1.36

In Fig. 2, we show the time evolution of the ALP production rate integrated over energies for the SN models described in Sec. II. For failed CC SN explosions, the flux quickly rises and is abruptly terminated when a black hole is formed, at post-bounce times $t_{\text{pb}} = 1 \text{ s}$ for $40 M_\odot$ progenitor and at $t_{\text{pb}} = 0.1 \text{ s}$ for the $70 M_\odot$ progenitor. Instead, for the successful CC SN explosion models the ALP signal reaches the peak at $t_{\text{pb}} \gtrsim 1 \text{ s}$: the larger the post-bounce time the heavier the progenitor. In particular, for the exploding models the time evolution of the energy-integrated ALPs number luminosities is well reproduced by the following analytical expression

$$\frac{dN_a}{dt} = a \left(\frac{g_{a\gamma}}{10^{-11} \text{ GeV}^{-1}} \right)^2 \left(\frac{t}{s} \right)^b \exp(-ct). \quad (3)$$

The values of the parameters are given in Table I for different SN progenitors. Assuming $m_a \ll T$, the time integrated ALP spectrum is given, with excellent precision, by the analytical expression [10]

$$\frac{dN_a}{dE} = C \left(\frac{g_{a\gamma}}{10^{-11} \text{ GeV}^{-1}} \right)^2 \left(\frac{E}{E_0} \right)^\beta \exp \left(-\frac{(\beta+1)E}{E_0} \right). \quad (4)$$

where the values of the parameters C , E_0 , and β for the SN models with different progenitors are given in Table II. The spectrum described in Eq. (4) is a typical quasi-thermal spectrum, with mean energy E_0 and index β (in particular, $\beta = 2$ would correspond to a perfectly thermal spectrum of ultrarelativistic particles).

In Fig. 3, we represent the SN ALP energy flux from different progenitors. We realize that for the successful CC SN explosions the average energy E_0 increases monotonically with the progenitor mass, as well as the peak

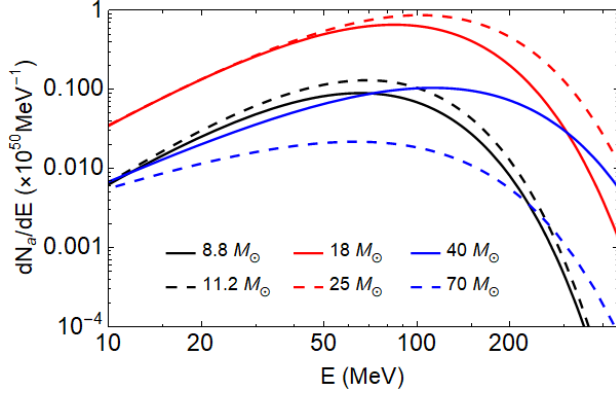


FIG. 3. SN ALP number flux in function of energy for different SN progenitor mass. We assume $m_a \ll 10^{-11}$ eV and $g_{a\gamma} = 10^{-11}$ GeV $^{-1}$.

of the spectrum. Conversely for the failed CC SN explosions, since the emitted flux is integrated over a shorter time window, the flux is suppressed with respect to the previous models.

For further purposes related to the calculation of the DSNALPB it is useful to determine the variation of the spectral coefficients C , E_0 , and β in function of the SN progenitor mass. Given the sparseness of the data we assume a linear behaviour in the range $[8; 30] M_\odot$, as shown in Fig. 4. The functional expressions are the following ones

$$\begin{aligned} \frac{C(M)}{10^{50} \text{ MeV}^{-1}} &= (1.06 \pm 0.191) \frac{M}{M_\odot} - 6.08 \pm 3.25, \\ \frac{E_0(M)}{\text{MeV}} &= (3.64 \pm 0.255) \frac{M}{M_\odot} + 55.8 \pm 4.32, \\ \beta(M) &= (-0.0280 \pm 0.0119) \frac{M}{M_\odot} + 2.93 \pm 0.201. \end{aligned} \quad (5)$$

For failed CC SN explosions, we only have two models from different groups, and therefore we do not attempt any interpolation.

B. Diffuse SN ALP background

From the SN ALP flux described in the previous section, one can calculate the DSNALPB from all past CC SNe in the Universe, as in [16] (see also [15, 50]),

$$\frac{d\phi_a(E_a)}{dE_a} = \int_0^\infty (1+z) \frac{dN_a^{CC}(E_a(1+z))}{dE_a} [R_{SN}(z)] \left[c \frac{dt}{dz} \right] dz \quad (6)$$

where z is the redshift, $R_{SN}(z)$ is the SN explosion rate and $|dt/dz|^{-1} = H_0(1+z)[\Omega_\Lambda + \Omega_M(1+z)^3]^{1/2}$ with the cosmological parameters $H_0 = 67.4$ km s $^{-1}$ Mpc $^{-1}$, $\Omega_M = 0.315$, $\Omega_\Lambda = 0.685$ [51]. The spectrum dN_a^{CC}/dE_a represents the ALP emission from all past CC SN events.

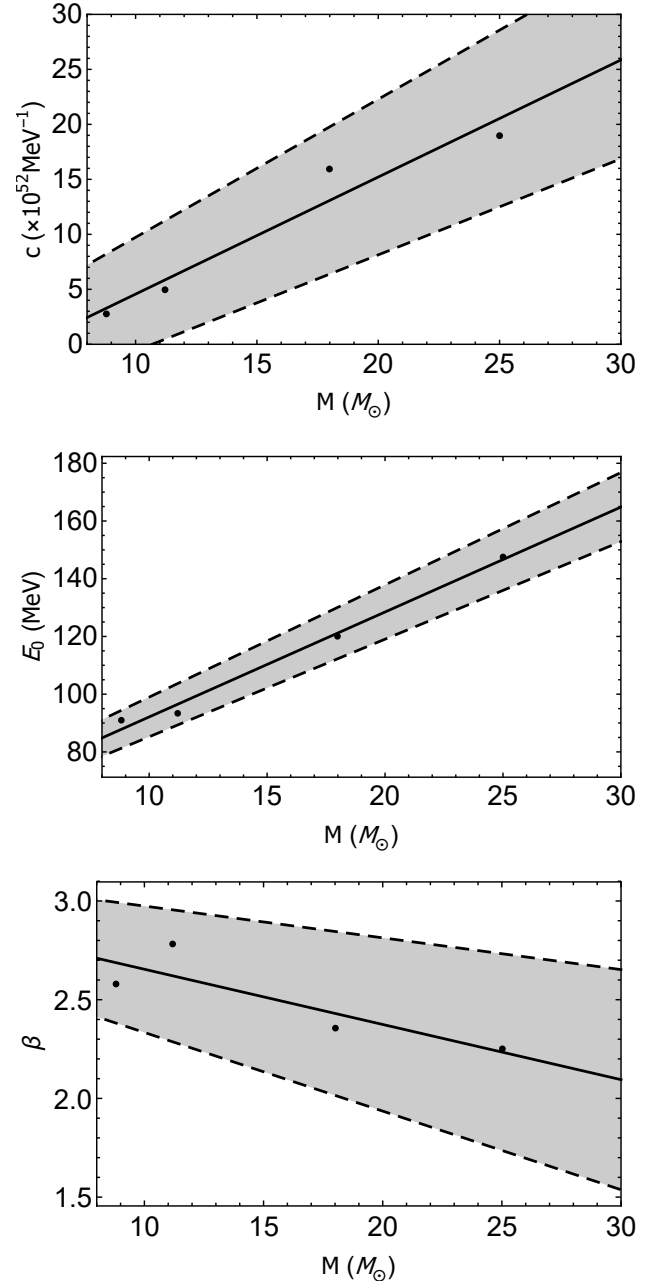


FIG. 4. Variation of spectral parameters of Eq. (4) as a function of the SN progenitor mass. We assume $m_a \ll 10^{-11}$ eV and $g_{a\gamma} = 10^{-11}$ GeV $^{-1}$. The gray area represents the uncertainties on the spectral parameters and on the SNR.

ALP spectrum from past core-collapse SNe. In order to calculate the ALP spectrum of past CC SN events dN_a^{CC}/dE_a , one has to weight the flux from a given CC SN over the initial mass function (IMF) which provides the number of stars formed per unit of mass as function of the progenitor mass M .

Following [52–54], we apply the modified Salpeter-A IMF of [55]

$$\phi(M) \propto M^{-\zeta}, \quad (7)$$

with $\zeta = 2.35$ for birth masses $M \gtrsim 0.5M_\odot$, and $\zeta = 1.5$ for $0.1M_\odot \leq M \leq 0.5M_\odot$. It is expected that the IMF of stars may depend systematically on the environment. In this context, in Ref. [56] it was suggested to empirically investigate the effect of metallicity changing the exponent ζ in a range $[0.34 : 3.44]$. We find that the effect can produce a factor ~ 2 change in the DNSALPB flux.

$$\frac{dN_a^{CC}}{dE_a} = \frac{\int_{\Lambda_{\text{expl-CC}}} dM \phi(M) \frac{dN_a}{dE}(M) + \int_{\Lambda_{\text{fail-CC}}} dM \phi(M) \frac{dN_a}{dE}(M)}{\int_{8M_\odot}^{125M_\odot} dM \phi(M)}, \quad (8)$$

where $\Lambda_{\text{expl-CC}}$ and $\Lambda_{\text{fail-CC}}$ represent the domains in the progenitor mass range where one expects to have a successful and a failed CC SN explosion progenitor, respectively. In particular, the domain of failed CC SN explosions is defined following [58]:

$$f_{\text{fail-CC}} = \frac{\int_{\Lambda_{\text{fail-CC}}} dM \phi(M)}{\int_{8M_\odot}^{125M_\odot} dM \phi(M)}, \quad (9)$$

and implemented here as an hard cut $M_{\text{fail-CC}}^{\text{min}}$, which represents the lower mass bound of the failed CC SN explosions domain. From here, it also follows that $f_{\text{expl-CC}} = 1 - f_{\text{fail-CC}}$.

In order to study the DSNALPB sensitivity to $f_{\text{fail-CC}}$ we consider four different scenarios, as in [58]. Each scenario is characterized by a different $M_{\text{fail-CC}}^{\text{min}}$. We consider that all stars with $M > M_{\text{fail-CC}}^{\text{min}}$ evolve into BH-SNe. For progenitor masses lower than $M_{\text{fail-CC}}^{\text{min}}$ we assume successful explosions with spectrum in Eq. (4) following the scaling of the parameters given by Eq. (5). Instead, we model failed CC SNe explosions as the $40 M_\odot$ model for $M_{\text{fail-CC}}^{\text{min}} < M < 60 M_\odot$. In the range $[60 : 125]M_\odot$ they are represented by the $70M_\odot$ model. The four scenarios are:

- $f_{\text{fail-CC}} = 10\%$: $M_{\text{fail-CC}}^{\text{min}} = 36M_\odot$, see e.g. [38, 59]. This is a (as concerns ALPs) optimistic scenario where the fraction of SNe leading to black hole formation is small.
- $f_{\text{fail-CC}} = 20\%$: $M_{\text{fail-CC}}^{\text{min}} = 24.0 M_\odot$, following Refs. [60, 61].
- $f_{\text{fail-SN}} = 30\%$: $M_{\text{fail-CC}}^{\text{min}} = 18.5 M_\odot$.
- $f_{\text{fail-SN}} = 40\%$: $M_{\text{fail-CC}}^{\text{min}} = 15.0 M_\odot$. This is based on the findings of Ref. [62, 63] and it is still well within the observational constraints [64].

In principle, it has been recently shown that the appearance of exotic phases of hot and dense matter, associated with a sufficiently strong phase transition from nuclear matter to the quark-gluon plasma at high baryon density, can trigger supernova explosions of massive stars

In our study, we consider masses from 8 up to $125 M_\odot$. However, due to the steep decline of Eq. (7), the high-mass end is suppressed and thus of minor relevance for the DSNALPB. The IMF-weighted ALP spectrum dN_a^{CC}/dE_a of all CC SN events can then be calculated as [57]

in the range $35 - 50 M_\odot$. However, from nucleosynthesis studies it results that the contribution of these exotic SNe might be at most 1 % of the total ones [65]. Therefore, their contribution to the DSNALPB is negligible and we will neglect it hereafter.

Supernova rate R_{SN} . The intensity and spectrum of the DSNALPB depend on the cosmological rate of core collapse (or, shortly, Supernova Rate, SNR). The SNR, differential in the progenitor mass M , is proportional to the star formation rate (SFR), $R_{\text{SF}}(z)$ (defined as the mass that forms stars per unit comoving volume per unit time, at redshift z) [57]:

$$R_{\text{SN}}(z, M) = R_{\text{SF}}(z) \frac{\int_{8.0M_\odot}^{125M_\odot} dM \phi(M)}{\int_{0.5M_\odot}^{125M_\odot} dM M \phi(M)}. \quad (10)$$

The SFR is well described by the functional fit [52]

$$R_{\text{SF}}(z) = R_{\text{SF}}(0) \begin{cases} (1+z)^\beta & 0 < z < 1, \\ 2^{\beta-\alpha}(1+z)^\alpha & 1 < z < 4.5, \\ 2^{\beta-\alpha}5.5^{\alpha-\gamma}(1+z)^\gamma & 4.5 < z < 5. \end{cases} \quad (11)$$

where $\alpha = -0.26$, $\beta = 3.28$, $\gamma = -7.8$ and $R_{\text{SF}}(0) = \mathcal{O}(10^{-2})M_\odot\text{Mpc}^{-3}\text{yr}^{-1}$. Following [66], we take the total SNR to be $R_{\text{SN}}(0) = \int_{8M_\odot}^{125M_\odot} dM R_{\text{SN}}(0, M) = (1.25 \pm 0.5) \times 10^{-4}\text{yr}^{-1}\text{Mpc}^{-3}$.

DSNALPB flux. In Fig. 5 we show the DSNALPB fluxes for a photon coupling $g_{a\gamma} = 10^{-11} \text{ GeV}^{-1}$ and $m_a \ll 10^{-11} \text{ eV}$ for the different fractions of failed SNe $f_{\text{fail-CC}}$. We note the obvious that the larger $f_{\text{fail-CC}}$ the more suppressed is the flux. We also show the uncertainty on the flux due to the uncertainties on the spectral parameters and on the SNR (gray), and bracketed, from below, by the minimum flux for $f_{\text{fail-CC}} = 40\%$ and, from above, by the maximum flux for $f_{\text{fail-CC}} = 10\%$. Importantly, this implies that the estimated DSNALB flux may vary within a factor ~ 8 . For comparison we also show the flux obtained assuming that all SNe behave as the $18 M_\odot$ progenitor, as done in [16].

We find that also the DSNALPB spectrum can be represented by the functional form of Eq. (4). In Table III

TABLE III. Fitting parameters for DSNALPB fluxes for $g_{a\gamma} = 10^{-11} \text{ GeV}^{-1}$ and $m_a \ll 10^{-11} \text{ eV}$ for different fractions of failed SNe $f_{\text{fail-CC}}$.

$f_{\text{fail-CC}}$	$C [\times 10^{-7} \text{ MeV}^{-1} \text{ cm}^{-2} \text{ s}^{-1}]$	$E_0 [\text{MeV}]$	β
10% max flux	61.7	60.9	1.29
10%	44.1	60.9	1.29
20%	31.3	53.2	1.38
30%	21.9	52.2	1.34
40%	15.5	54.7	1.24
40% min flux	9.28	54.7	1.25

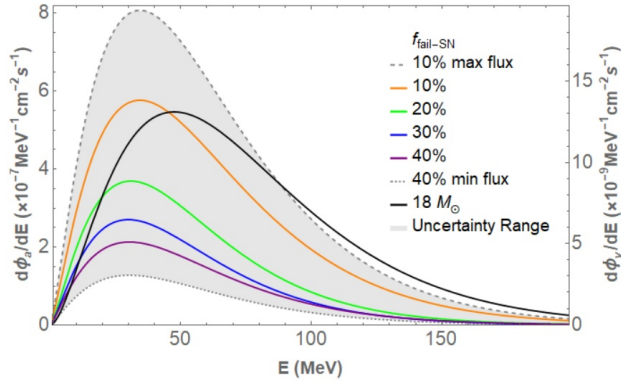


FIG. 5. DSNALPB fluxes for $g_{a\gamma} = 10^{-11} \text{ GeV}^{-1}$ and $m_a \ll 10^{-11} \text{ eV}$ for different fractions of failed SNe $f_{\text{fail-CC}}$. We also indicate the uncertainty on the flux due to the uncertainties on the spectral parameters and on the SNR (gray band). For comparison we display the flux obtained assuming that all SNe behave as the $18 M_{\odot}$ progenitor, as assumed in [16]. The right vertical axis refers to the photon flux observed from the direction $(b, l) = (-15^{\circ}, 30^{\circ})$ assuming the benchmark model of magnetic field.

we show the fitting parameters for the four cases with different $f_{\text{fail-CC}}$. Typically, in this case the average energy of the spectrum is $E_0 \sim 50 \text{ MeV}$.

DSNALPB gamma-ray flux. As pointed out in [16] The DSNALPB would convert into photons in the Galactic magnetic field, leading to a diffuse gamma-ray flux. We follow the characterization of ALP-photon conversions presented in [16] to which we address the interested reader for further details. In particular, the Galactic magnetic field model is described by the Jansson-Farrar model ([67]) with the updated parameters given in Tab. C.2 of [68] (“Jansson12c” ordered fields). This is our baseline model. Alternatively, to quantify the uncertainty on the magnetic field, the Pshirkov model [69] is used. This second model features a larger magnetic field in the Galactic plane and a weaker off-plane component. In both cases the electron density in the Galaxy is described by the model in [70]. The gamma-ray induced signal along a specific line of sight is represented in Fig. 5, right axis.

IV. FERMI-LAT ANALYSIS FRAMEWORK

A. Data selection

We use 12 years of *Fermi*-LAT Pass8 data. The signal is peaked at about 50 MeV. Therefore, we use two separate data sets with different selection criteria to specifically improve the analysis of LAT data below 200 MeV. The applied criteria are summarized in Tab. IV.

While the $E < 200 \text{ MeV}$ data is the main driver of the constraint, let us nevertheless start by describing our procedure for the more standard $E \geq 200 \text{ MeV}$ data set. This gives the picture of the main ingredients in our analysis. We will later comment on the adaptations for the $E < 200 \text{ MeV}$ region.

The data set of events $E \geq 200 \text{ MeV}$ includes both front- and back-converted events to increase the statistical sample, whereas the data set with $E < 200 \text{ MeV}$ is restricted to photons of the PSF3 event type. This decision has been made to benefit from the slightly better angular reconstruction efficiency of this event type compared to the generally poor angular resolution of the LAT at the lower end of its sensitivity range⁵. For both data sets the **ULTRACLEANVETO** event class has been chosen as it minimizes the contamination by misclassified cosmic-ray events, which is essential for studies of large-scale diffuse sources like the extragalactic ALP flux from SNe. The choice of this event class requires us to select the *Fermi*-LAT Instrument Response Functions (IRFs) **P8R3_ULTRACLEANVETO_V3** with which we will convolve the physical gamma-ray emission models to generate from them the expected number of photon events. The LAT data as well as the model data to be generated are stored as all-sky maps and binned according to the HEALPix pixelization scheme [71] with $N_{\text{side}} = 64$. The mean distance between the centers of two such HEALPix pixels amounts to about 0.9° . All data manipulations involving either the LAT data or the application of LAT IRFs is done via the Fermi Science Tools⁶ (version 2.0.8).

B. Methodology

The ALP-induced gamma-ray flux manifests itself as a large-scale contribution to the overall gamma-ray sky at low Galactic latitudes around the Galactic disc as well as at high Galactic latitudes. To do justice to this fact, we develop a template-based analysis that utilizes all-sky maps of the expected photon counts for various background components and the ALP signal template. The selection of astrophysical gamma-ray emission back-

⁵ The description of the LAT’s performance figures can be found at https://www.slac.stanford.edu/exp/glast/groups/canda/lat_Performance.htm

⁶ <https://github.com/fermi-lat/Fermitools-conda>

Data Set	$E < 200$ MeV	$E \geq 200$ MeV
Reconstruction algorithm	Pass 8	
Event class	ULTRACLEANVETO	
Event type	PSF3	FRONT+BACK
Energy range	50 MeV - 200 MeV	200 MeV - 500 GeV
Time interval	12 years (4th August 2008 - 3rd September 2020)	
ROI	all sky	
Zenith angle (applied to gtlcube)	$< 90^\circ$	
Time cuts filter	DATA_QUAL==1 && LAT_CONFIG==1	
HEALPix resolution	$N_{\text{side}} = 64$	
energy binning	30 logarithmically-spaced bins	

TABLE IV. Data selection and preparation specifications .

grounds comprises Galactic and extragalactic contributions that are commonly considered in studies of the LAT data. To give a rough outline of the analysis strategy, we first single out the region of the sky that yields the best agreement between a model built from the astrophysical emission components. In a second step, this region of interest is used to constrain the strength of the ALP-induced gamma-ray flux.

Astrophysical background model selection. The model for the gamma-ray sky is created from a selection of the “guaranteed” emission components on which we comment in the following. We process these models with the Fermi Science Tools and its dedicated routines; in particular, the routine *gtmodel* to derive photon count templates, i.e. templates convolved with the LAT’s PSF⁷ and multiplied by the exposure depending on the data set (see Tab. IV) to obtain the “infinite statistics” or *Asimov* dataset [72]. We incorporate in the analysis:

- Interstellar emission (IE) – the combined gamma-ray flux due to high-energy charged cosmic rays interacting with gas, photon radiation fields and dust in the Milky Way – which is represented by five distinct models to examine the robustness of the analysis with respect to variations of this particular component. From the wide range of different attempts to quantify the intensity, spatial and spectral structure of the Galactic interstellar emission, we choose as the benchmark in our analysis one particular model instance that has been created to examine the systematic uncertainty inherent to the “1st Fermi LAT Supernova Remnant Catalog” [73].⁸ In what follows, we will refer to

this model by “Lorimer I”. While the documentation of the exact details of this model can be found in the referenced publication [73], we stress here the basic assumptions underlying its construction: The sources of primary cosmic rays are assumed to follow the distribution of pulsars in the Milky Way as reported in [74]. The typical height of the cosmic-ray propagation halo is set to $z = 10$ kpc, while the spin temperature of the interstellar medium is taken to be $T = 150$ K. These model parameters and assumptions are not largely different from similar models that have in the past and recently been applied to study the characteristics of the gamma-ray emission in the Galactic center region [20, 23]. Another advantage of this model is its decomposition into an inverse Compton map and gas maps (notably atomic H as well as CO as a proxy for the distribution of H₂), which are themselves split into Galactocentric annuli of various extension (0-4 kpc: “ring 1”, 4-8 kpc: “ring 2”, 8-10 kpc: “ring 3” and 10-30 kpc: “ring 4”). This subdivision into annuli allows us to perform an optimization of the individual model components via an all-sky baseline fit which we describe later. We complement this benchmark choice with four additional interstellar emission models: “Lorimer II” – another model instance from [73] with the only difference from Lorimer I being an extreme choice for the spin temperature which is taken to be $T = 1 \cdot 10^5$ K as well as the “Foreground Models” A, B and C from the in-depth Fermi-LAT study of the diffuse extragalactic gamma-ray background [75].⁹ The interstellar emission models of the latter publication possess the advantageous feature of having been created with the idea in mind that they will eventually be used to study high-latitude LAT data; a task that we are likewise aiming at.

⁷ Fermi-LAT key performance figures

⁸ The model files have been made public by the *Fermi*-LAT collaboration: https://fermi.gsfc.nasa.gov/ssc/data/access/lat/1st_SNR_catalog/. We note that these files have been initially generated to be compatible with Pass7 LAT data. However, they may be manually converted to comply with the Pass8 standard by using the same factor that distinguishes the official *Fermi*-LAT diffuse background models *g11_iem.v05* and *g11_iem.v06*.

⁹ The relevant model files can be retrieved from the *Fermi*-LAT collaboration’s public data archive: https://www.glast.stanford.edu/pub_data/845/

- **Isotropic diffuse background (IGRB)** – The spatial morphology of this component follows the exposure of the LAT while its spectrum is determined in connection with a particular interstellar emission model. For our analysis, we adopt the IGRB component shipped with the Fermi Science Tools¹⁰ and respecting the choice of event class and type in the context of the two data sets in Tab. IV. Note that – due to reasons that will become clear later while describing the analysis routine – the adopted spectrum of the IGRB does not play a crucial role in our study.
- **Detected point-like and extended gamma-ray sources (PS)** – A *Fermi*-LAT analysis of 10 years of data has revealed more than 5700 individual gamma-ray sources inside and outside of the Milky Way [76, 77]. We include this latest iteration of a high-energy gamma-ray source catalog, the 4FGL-DR2, in our analysis. Depending on the analyzed data set, the treatment and handling of these detected sources may differ and the explicit description of our approach follows later in the text.
- **Fermi Bubbles (FBs)** – As a large-scale diffuse component that extends to high-latitudes in the northern and southern hemisphere of the projected gamma-ray sky, we incorporate the FBs as a template according to their spatial characterization provided in [20]. We adopt as their fiducial spectrum a log-parabola $\frac{dN}{dE} = F_0 \left(\frac{E}{E_0} \right)^{-\alpha - \beta \ln(E/E_0)}$ with parameters $F_0 = 5 \times 10^{-10} \text{ ph cm}^{-2} \text{ s}^{-1} \text{ MeV}^{-1}$, $\alpha = 1.6$, $\beta = 0.09$ and $E_0 = 1 \text{ GeV}$ taken from [78].
- **LoopI** – Another large-scale diffuse emission component, which is most prominently present in the northern hemisphere above the Galactic disc. We adopt the geometrical spatial structure (and spectral) as considered in the 1st Fermi-LAT SNR catalog analysis [73] that is based on a study in [79].
- **Gamma-ray emission from the Sun and the Moon (SUN)** – Both the Sun and the Moon can contribute a sizeable gamma-ray background when they pass through the region of interest of a particular analysis. Since we are aiming to conduct an all-sky study, their emission must be taken into consideration. The Fermi Science Tools offer routines¹¹ to calculate a LAT data-based Sun and Moon gamma-ray template via the techniques presented in [80].

Statistical inference procedure. The grand scheme of this analysis is an all-sky template-based fit. To this end, we construct a fitting routine that utilizes the Poisson likelihood function subdivided into energy bins i and spatial pixels p

$$\mathcal{L}(\boldsymbol{\mu} | \boldsymbol{n}) = \prod_{i,p} \frac{\mu_{ip}^{n_{ip}}}{(n_{ip})!} e^{-\mu_{ip}} \quad (12)$$

for binned model data $\boldsymbol{\mu}$ and experimental data \boldsymbol{n} . The model data are a linear combination of the templates \boldsymbol{X} introduced above

$$\boldsymbol{\mu} = G_a \boldsymbol{X}^{\text{ALP}} + \sum_X \sum_i A_i^X X_i \quad (13)$$

where $X \in \{\text{IE, IGRB, PS, FB, LoopI, SUN}\}$. This construction introduces two kinds of normalization parameters. The first are a set of normalization parameters, A_i^X , for each energy bin of each astrophysical background component. These parameters can be varied independently of each other during a fitting step. The advantage of such an approach is that spectral imperfections of the original astrophysical emission models are less impactful as they are re-adjusted in a fit. Thus, a greater emphasis is given to the spatial morphology of the background components. This technique has been successfully applied in previous studies, e.g. [20, 81]. Second, the signal component, i.e. the ALP-induced gamma-ray flux, is modelled with a single, global normalization parameter G_a since we aim to exploit both the spatial and spectral shape of this component. To re-iterate the discussion of the ALP signal in Sec. IIIB, its spectral shape is dictated by the physics of core-collapse SNe while the spatial morphology is a direct consequence of the shape of the Galactic magnetic field of the Milky Way. Note that while the importance of the spectral shape of each background component is reduced, a similar statement about the ALP signal's spectrum is not correct. Therefore, we need to include energy dispersion¹² during the generation of the signal template with the Fermi Science Tools. The impact of energy dispersion is growing with decreasing photon energy and highly recommended at energies below 100 MeV. Therefore, we use `edisp_bins=-2` (two additional energy bins are added below and above the nominal energy range of the data set to compute spectral distortions due to energy dispersion effects) for the data set of $E < 200 \text{ MeV}$ and `edisp_bins=-1` for the data set of $E \geq 200 \text{ MeV}$ with `apply_edisp=true` in the spectrum part of the input to the Fermi Science Tools.

We infer the best-fit parameters of the model with respect to one of the LAT data sets via the maximum like-

¹⁰ The relevant spectrum files are also provided at <https://fermi.gsfc.nasa.gov/ssc/data/access/lat/BackgroundModels.html>

¹¹ An explanation is provided under https://fermi.gsfc.nasa.gov/ssc/data/analysis/scitools/solar_template.html

¹² The Pass 8 reconstruction standard has revealed that energy dispersion effects are a crucial ingredient to realistically simulate LAT observations. More information on this subject are provided at this website: https://fermi.gsfc.nasa.gov/ssc/data/analysis/documentation/Pass8_edisp_usage.html

likelihood method for which we invoke the weighted logarithmic Poisson likelihood [76]

$$\ln \mathcal{L}_w(\boldsymbol{\mu}|\mathbf{n}) = \sum_{i,p} w_{ip} (n_{ip} \ln \mu_{ip} - \mu_{ip}). \quad (14)$$

This weighted log-likelihood function has been introduced by the *Fermi*-LAT collaboration in connection with the generation of the 4FGL catalog as to incorporate the impact of systematic uncertainties on the analysis results. The basic idea is to assign to each pixel (per energy bin) a weight – a quantity that is essentially obtained via integration in space and energy of the provided model or LAT data – in order to suppress the statistical impact of certain parts of the target region where the emission is dominated by systematic uncertainties. An exhaustive discussion of the calculation and properties of these weights can be found in Appendix B of [76]¹³. The numerical routines (`gteffbkg`, `gtalpbkg`, `gtwtsmap`) to

compute the weights for a particular setup are part of the Fermi Science Tools.

As concerns this analysis, we choose to incorporate “data-driven” weights in our analysis pipeline. These weights are directly computed from the selected LAT data. Hence, they yield a means to penalize pixels that suffer from systematic effects like misclassified charged cosmic-ray events, PSF calibration, IE spectral modeling uncertainties in bright regions of the sky or sky parts hosting particularly bright point-like sources that overshadow their surroundings. We fix the level of the assumed systematic uncertainties to 3% (for all energy bins), which is the fiducial value utilized and tested for the creation of the 4FGL source catalog [76]. The likelihood maximization step is performed with the `IMINUIT` python package [82] and the `migrad` minimization algorithm it provides.

To discriminate between different hypotheses – quantifying a possible preference for the model in Eq. 13 with or without an ALP emission component – we employ the log-likelihood ratio test statistic

$$\text{TS}(G_a) = \begin{cases} -2 \min_{\{A_i^x\}} \left(\ln \left[\frac{\mathcal{L}_w(\boldsymbol{\mu}(G_a, A_i^x) | \mathbf{n})}{\mathcal{L}_w(\hat{\boldsymbol{\mu}} | \mathbf{n})} \right] \right) & G_a \geq \hat{G}_a \\ 0 & G_a < \hat{G}_a \end{cases} \quad (15)$$

by adopting the construction discussed in [72]. In our case at hand, the astrophysical background normalization parameters are treated as nuisance parameters and $\hat{\cdot}$ denotes the best-fit values of signal and background normalization parameters. In the case of no significant ALP signal, this test statistic allows us to set upper limits on the ALP normalization parameter. As Eq. (15) only depends on one parameter and values of G_a smaller than the best-fit value are discarded, its distribution follows a half- χ^2 -distribution with one degree of freedom (see Sec. 3.6 of [72]). Consequently (still following the calculations in the mentioned reference), an 95% CL upper limit on G_a can be set where the test statistic attains a value of 2.71.

Fitting procedure. To derive an upper limit on the strength of the ALP-induced gamma-ray flux, we have to face and solve two main challenges:

1. What is the part of the sky that yields the best agreement between a model consisting of the six emission components introduced in the previous section and the measured LAT data? Only such a region of interest can be exploited in order to

constrain the ALP signal strength in a statistically sound approach. The manner in which this optimization process is performed was inspired by the approach presented in [83], where the authors aim to constrain weakly interacting massive particles via a gamma-ray signal from the Milky Way’s outer dark matter halo.

2. How do we have to adapt our fitting procedure to the particular case of the two data sets above and below 200 MeV? The main concern of the data set below 200 MeV is the large PSF size of the instrument, which heavily impacts the manner to incorporate the population of detected gamma-ray sources from the 4FGL catalog.

The subsequent paragraphs are presenting the reasoning that applies to the LAT data set above 200 MeV. After this general outline of our approach, we comment on the parts that need to be altered when handling the data set below 200 MeV.

To answer the first point raised, we adopt and adapt the iterative all-sky fitting strategy that has been proposed and applied by the Fermi-LAT collaboration to derive the current iteration of their Galactic diffuse background model¹⁴. In the companion publication¹⁵ that

¹³ Another source that explains this weighted likelihood approach is found at: https://fermi.gsfc.nasa.gov/ssc/data/analysis/scitools/weighted_like.pdf

¹⁴ The model file can be downloaded from this website:

describes the details of the collaboration’s analysis, an outline of the general procedure is given in Sec. 4: The main idea is to perform a maximum likelihood fit utilising Eq. 14 (and fixed $G_a = 0$) by selecting characteristic sky regions where only a few components would dominate while the sub-dominant components remain fixed to initial normalization values or the results of previous iteration rounds. In what follows, we list the definitions of the different sky regions that we consider in our work and those templates – with respect to our benchmark IEM “Lorimer I” – that are left free therein (masks corresponding to the chosen regions are shown in Fig. 6):

1. *High-latitude*: $|b| > 30^\circ$ and without the “patch”-region, which we define as $-105^\circ \leq \ell \leq 60^\circ$. The patch region is the part of the sky where Loop I and the FBs are brightest. Here, we leave free the following templates: HI ring 3, IC, 4FGL, IGRB and Sun.
2. *Outer galaxy*: $|b| \leq 30^\circ$, $|\ell| > 90^\circ$. This concerns the following templates: 4FGL, HI ring 4, CO ring 4 and IC.
3. *Inner galaxy*: $|b| \leq 30^\circ$, $|\ell| \leq 90^\circ$. This concerns the following templates: 4FGL, HI ring 1, HI ring 2, CO ring 1, CO ring 2, CO ring 3 and IC.
4. *Patch region/all-sky*: To adjust the normalization parameters of the Loop I and FB templates, we fit them on the full sky while all other templates are fixed.

After iterating this procedure 100 times, we have obtained a *baseline fit* to the LAT data with which we perform the tests of statistical robustness of certain regions of interest in the following. Moreover, this routine provides us with a data-optimized IEM that we create by summing the gas and IC components with their respective best-fit normalization factors. To avoid fitting all gas rings every time, we use this optimized IEM as a single template in what follows. Note that only the IE models “Lorimer I” and “Lorimer II” enable a fit with split gas rings whereas foreground models A, B and C are treated differently. To conduct the baseline fit in their case, we split the single IE template into three independent parts coinciding with the definitions of the sky patches of the iterative fit. The same reasoning is also applied to the IC template for all five IEMs.

Region of interest optimization. Consequently, we systematically search for a region of interest that provides statistically reliable upper limits on the ALP signal’s

strength. To this end, we exclusively resort to the southern hemisphere as to avoid possible contamination by the gamma-ray emission of the rather poorly constrained Loop I - structure. In addition – to reduce the human bias on the optimization process of the ROI – we exchange the physical gamma-ray spectrum of the diffuse ALP background with a simple power law of spectral index -2 .¹⁶ We fix its reference flux normalization A^{ALP} so that the resulting flux is one order of magnitude lower than the DSNALPB at a reference energy of 100 MeV and ALP-photon coupling of $g_{a\gamma} = 5.3 \times 10^{-11} \text{ GeV}^{-1}$ corresponding to the limit derived in [16]. Consequently, the maximal photon counts per pixel are of order unity at this reference energy. By invoking Eq. 15 (replacing $G_a \rightarrow A^{\text{ALP}}$) and including the ALP template with a non-zero normalization, we derive the associated TS-distribution in a particular region of the sky, which we systematically shrink from $\ell \in [-180^\circ, 180^\circ]$ to $\ell \in [-90^\circ, 90^\circ]$ with $b \in [-90^\circ, -30^\circ]$. The cut in Galactic latitude is applied to reduce the impact of the IE along the Galactic disc. For all tested sky regions, we compare the resulting TS-distributions for input data \mathbf{n} that are either a particular LAT data set or the baseline fit data with respect to the IEM Lorimer I. The latter data set has to advantage of allowing us to draw Poisson realizations that eventually show the scatter of the expected upper limits on A^{ALP} . This optimization procedure leads us to the choice of the region of interest for the analysis, presented in Sec. V. We stress that A_{ALP} is an auxiliary parameter whose baseline value is connected to the ALPs expected gamma-ray brightness, and used to tune the analysis pipeline.

Treatment of detected sources in the 4FGL catalog. Besides the (ℓ, b) -mask to inspect the admissibility of a particular region of interest in the southern hemisphere, we are also masking the positions of all detected gamma-ray sources that are listed in the 4FGL catalog. Each source is masked in a circular region centered on their nominal position in 4FGL with a radius that corresponds to the 95% containment radius of the LAT’s PSF at a given energy. The source mask radius is extended by the reported extension of a source when applicable. However, this reasoning would lead to masking the entire sky at energies $E \lesssim 500 \text{ MeV}$. Hence, we only use the 68% containment radius for the respective energy bins. We have checked that increasing the mask radii at these energies does not impact the final results.

Adjustements for the data set $E \leq 200 \text{ MeV}$. While the overall rationale of the fitting procedure remains the same, there are a number of necessary changes to be made in order to optimize the analysis pipeline at the lowest

<https://fermi.gsfc.nasa.gov/ssc/data/access/lat/BackgroundModels.html>

¹⁵ https://fermi.gsfc.nasa.gov/ssc/data/analysis/software/aux/4fgl/Galactic_Diffuse_Emission_Model_for_the_4FGL_Catalog_Analysis.pdf

¹⁶ We ensure that the integrated spatial part of the map is equal to 1 (normalized), resulting in a power law flux normalization $N_0 = 5.8 \times 10^{-11} \text{ cm}^{-2}\text{s}^{-1}\text{MeV}^{-1}\text{sr}^{-1}$ at a reference energy of $E_0 = 100 \text{ MeV}$.

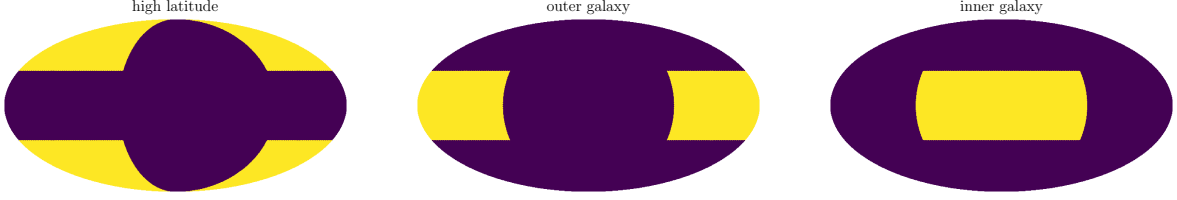


FIG. 6. The regions of interest (yellow) used for the iterative all-sky fitting pipeline, in Mollweide projection; see text for the definitions of the regions.

energies accessible to the Fermi LAT. The LAT’s PSF size rapidly deteriorates at these energies to values larger than one degree. On the one hand, while bright gamma-ray sources can still be identified as individual sources, the vast majority of sources listed in 4FGL will create a sea of photons that rather seems to be of a diffuse origin and, thus, increasing the degeneracy with genuinely diffuse signals like the ALP-induced gamma-ray flux. On the other hand, the ALP signal’s spectrum attains its maximal values around 50 to 100 MeV so that this energy range is expected to yield the strongest constraints.

To account for these obstacles, we first modify the baseline fit routine: Instead of using a single 4FGL template that encompasses all detected sources, we split the full template into eight individual templates defined by the number of expected photons per source N_γ within the energy range of the LAT data set, i.e. $E \in [50, 200]$ MeV. The estimate of N_γ per source follows from the best-fit spectrum as reported in the catalog and the LAT exposure. The defining lower and upper boundaries of each template are:

- $N_\gamma < 1$,
- $1 \leq N_\gamma < 10$,
- $10 \leq N_\gamma < 50$,
- $50 \leq N_\gamma < 100$,
- $100 \leq N_\gamma < 200$,
- $200 \leq N_\gamma < 500$,
- $N_\gamma \geq 500$ without the ten brightest sources,
- extended sources,
- each of the ten brightest sources is fit individually.

Since the brightest sources in the gamma-ray sky may substantially impact the quality of the fit, we single out the ten brightest sources below 200 MeV and fit them individually with the rest of the aforementioned 4FGL templates – leaving their normalization free only in those regions of the iterative fit where they are present. After the baseline fit has converged these ten sources are added to the template with $N_\gamma \geq 500$. The resulting all-sky

baseline fit and IEM data is henceforth utilized in the same way as it was done in the case of the first LAT data set.

A second adjustment concerns the systematic search for a suitable region of interest: This data set consists of 30 energy bins – mainly to guarantee a sufficient sampling of the LAT IRFs and energy dispersion. While the baseline fit has been conducted with the full number of energy bins, we rebin this data set to larger macro bins in all later stages of the analysis. The number of macro bins is a hyperparameter that needs to be optimized, too. Moreover, only a small fraction of the detected sources can be masked. The idea is to define a threshold for each energy bin in terms of number of expected emitted photons $N_{\text{thr},i}$. If a source exceeds this number, it has to be masked with a circular mask at 95% containment radius of the LAT’s PSF¹⁷. This will have an impact on the compatibility of LAT data and the baseline fit data. Hence, we scan over different high-latitude ROI masks as well as different values for $N_{\text{thr},i}$ and assess the deviation of LAT data’s and baseline fit data’s TS-distributions energy bin by energy bin. Eventually, we select those ROI masks and threshold values that produce the statistically most sound masks.

Combining the constraints from both data sets. Despite the fact that the fitting procedures are adapted individually for each data set, we can nonetheless derive a combined constraint on the ALPs’ signal strength via a joint-likelihood approach. Eq. 15 is valid in both cases and the signal templates are generated from the same input model. Thus, the normalization parameter A^{ALP} has the same meaning for both data sets. The joint-likelihood that we utilize within our framework is hence the sum of both weighted likelihood functions.

¹⁷ The PSF size in each macro bin is evaluated at the lowest energy among the micro bins that are contained in it.

V. RESULTS

A. Suitable regions of interest

Following the recipes outlined in Sec. IV B to single out a suitable analysis region for both LAT data sets, we present here the final results of this search. We stress again that in the context of this optimization step the IE is represented by the Lorimer I model.

In Fig. 7 we display the comparison of the TS-distributions obtained from the LAT data set under study (red) and the baseline fit model (black). The scatter of the TS-distribution is shown as 1σ and 2σ containment bands. The left panel of this figure refers to the data set with $E \geq 200$ MeV, for which we find the best agreement between real data and model for a region of interest with $-90^\circ < b < -30^\circ, |\ell| \leq 150^\circ$. The right panel of the same figure shows the situation for the data set below 200 MeV using six macro energy bins. The minimal deviation of LAT data and baseline fit model TS-distribution is ensured by using the 4FGL source mask threshold values $N_{\text{thr}} = (150, 110, 80, 110, 60, 40)$ with $\ell_{\text{max}} = 180^\circ$ for all but the first energy bin where $\ell_{\text{max}} = 90^\circ$ optimizes the agreement. Again, the Galactic latitude is set to $-90^\circ < b < -30^\circ$ to reduce the impact of the IE.

B. Upper limits on the ALP parameter space

After having determined in Sec. V A the region of interest that yields the most statistically sound upper limits on the ALP signal, we are able to set upper limits on the normalization parameter G_a of the signal template. Before that, we have checked that the selected parts of the sky do not contain a significant fraction of the ALP signal that would warrant a detection. We “unblind” our previous fitting routine by inserting the true signal template with the gamma-ray flux spectrum induced by ALPs from core-collapse SNe, Sec. III B; hence, the re-introduction of the normalization parameter G_a . We consider the DNALPB gamma-ray spectrum, propagating the uncertainty band in Fig. 5. We consider ALPs only coupled to photons. In this case, the upper limit on G_a translates into an upper limit on the photon-ALP coupling strength via $g_{a\gamma} = \sqrt[4]{G_a} g_{a\gamma}^{\text{ref}}$, where $g_{a\gamma}^{\text{ref}} = 5 \times 10^{-12} \text{ GeV}^{-1}$ refers to the reference value of the coupling at which spectrum and ALP-photon conversion probability in the Milky Way have been calculated to obtained the ALP template.

In Fig. 8 we show the resulting upper limits and confront those values with existing limits on the ALP parameter space. The displayed upper limits are based on the ALP signal morphology due to the Jansson model [84] of the Milky Way’s Galactic magnetic field and the iteratively optimized IEM Lorimer I. The red band represents the uncertainties on the DSNALPB gamma-ray spectrum due to the different scenarios of the ratio of

failed to successful CC SNe, i.e. this band is the one-to-one translation of the uncertainty band in Fig. 5 to an uncertainty on the upper limits on $g_{a\gamma}$.

In this setting, we find an improvement of the upper limit on $g_{a\gamma}$ regarding our previous analysis [16] that was solely based on the spectral shape of the ALP-induced gamma-ray flux. In numbers, we obtain $g_{a\gamma} \lesssim [2.2, 3.8] \cdot 10^{-11} \text{ GeV}^{-1}$ for ALP masses $m_a \ll 10^{-11} \text{ eV}$, depending on the assumed scenario for the ratio of failed to successful CC SNe.

Finally, let us note that the whole procedure can easily be applied also to other production mechanisms. For example, if we also consider a coupling between ALPs and nucleons, the limit on the ALP-photon coupling is significantly improved. In our analysis set-up – assuming $g_{aN} = 10^{-9}$ and very naively the same factor of improvement found in [16] – we obtain $g_{a\gamma} \lesssim 5.5 \cdot 10^{-14} \text{ GeV}^{-1}$ for ALP masses $m_a \ll 10^{-11} \text{ eV}$ regarding the most optimistic of our $f_{\text{fail-CC}}$ scenarios.

VI. DISCUSSION

We here discuss the astrophysical modelling uncertainties which affect the robustness of the limits, i.e. the modelling of the Galactic magnetic field, and the choice of the IE model.

A. Impact of the Galactic magnetic field model

To assess the robustness of the upper limits presented in Sec. V against different assumptions and models of the Milky Way’s magnetic field, we create a sample of alternative signal templates which have been taken from a recent study of the PLANCK collaboration [85] (Tab. 3.1 therein) and [88].

A comparison of the upper limits obtained from these models is displayed in Fig. 9. In general, different Galactic magnetic field models induce a variation in the derived upper limits on $g_{a\gamma}$ of $\mathcal{O}(1)$.

B. Impact of the Galactic diffuse foreground model

Although the ROI optimising has been conducted in the high-latitude gamma-ray sky to minimize the contamination by the Milky Way’s diffuse foreground emission, we investigate the robustness of the upper limits shown in Sec. V against variations of the Galactic foreground. To this end, we re-run the analysis pipeline with respect to the alternative interstellar emission models introduced in Sec. IV B.

The results of this cross-check are presented in Fig. 10. Variations of the IE have a smaller impact than model uncertainties in the magnetic field of the Milky Way. On one side, this implies that our analysis pipeline is robust

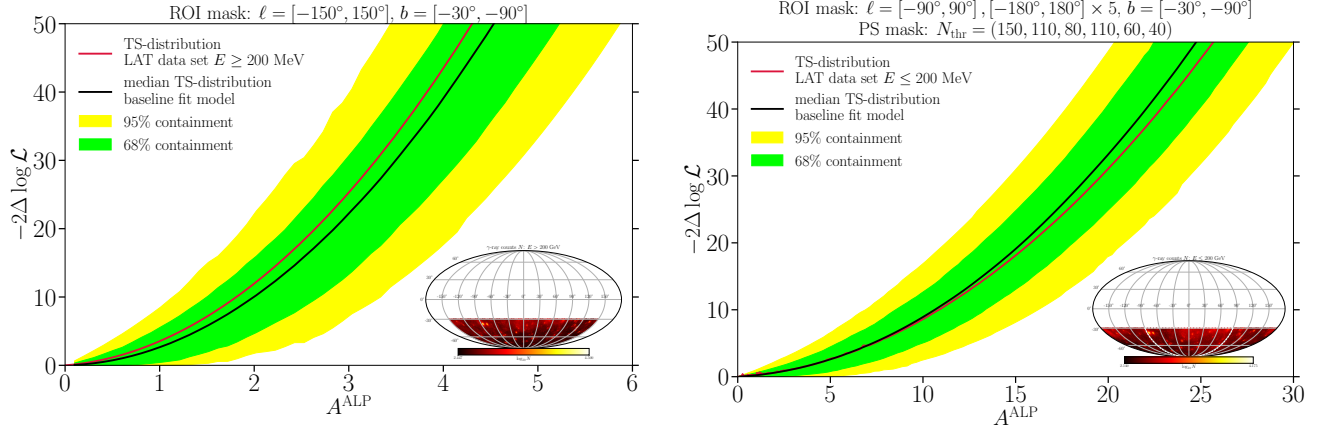


FIG. 7. (*Left:*) TS-distribution with respect to the baseline fit model (based on Lorimer I; black) and its statistical scatter (green: 68% containment, yellow: 95% containment) as well as the TS distribution with respect to the 12-year Fermi-LAT data including energies above 200 MeV (red). (*Right:*) Same as the left panel with respect to the LAT data set of events with $E \leq 200$ MeV. The fitting procedure uses six macro energy bins. In the lower right corner of each panel we display the optimized ROI showing the total gamma-ray counts in the respective data set projected on the sky.

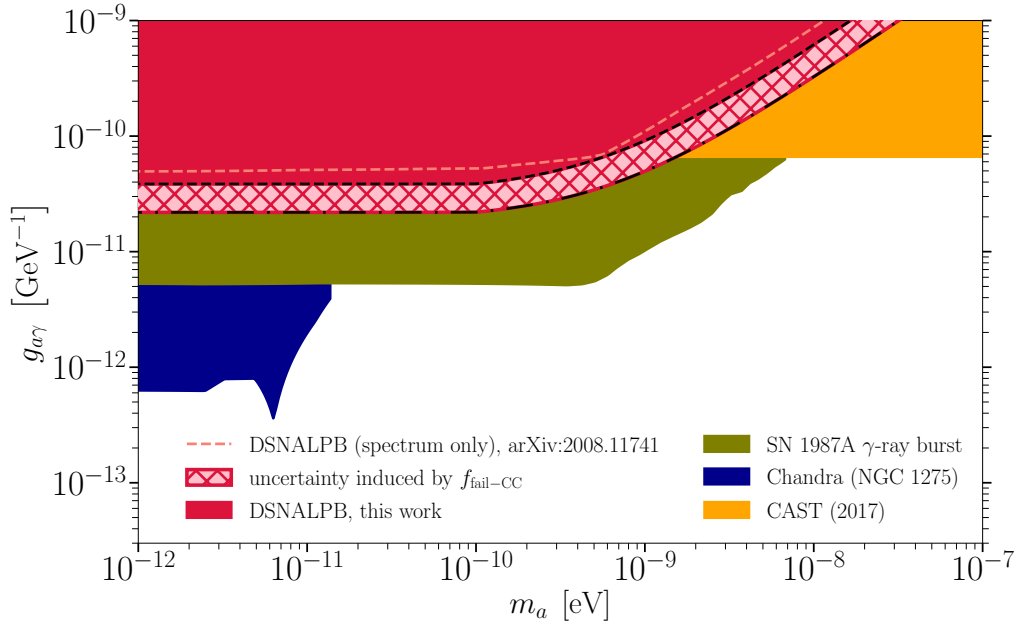


FIG. 8. Upper limits (red band) on the ALP-photon coupling constant $g_{a\gamma}$ assuming a coupling exclusively to photons and the ‘Jansson12c’ [85] model of the Milky Way’s Galactic magnetic field. The displayed band reflects the uncertainty on the DSNALPB gamma-ray spectrum caused by the unknown ratio of failed to successful CCSNe within the mass range of SN progenitors considered in this analysis (see Sec. III B). The width of the band is such that it encompasses all scenarios listed in Tab. III). To highlight the improvement of the upper limits regarding a previous analysis solely based on the expected spectral shape of the DSNALPB gamma-ray flux [16], we show this result as a dashed, light-red line. Our results are complemented by independent astrophysical and helioscope bounds on the ALP-photon coupling strength from CAST [86], Chandra observations of NGC 1275 [87] as well as the non-observation of a gamma-ray burst following SN 1987A [10].

against such alterations while, on the other side, it is essential to improve the existing models of the Galactic magnetic field, in particular, at high-latitudes.

VII. CONCLUSION

In this work, we carried out a comprehensive analysis of the gamma-ray diffuse signal induced by axion-like particles (ALPs) produced by all past cosmic core-collapse supernovae (CC SNe) and converted into high-

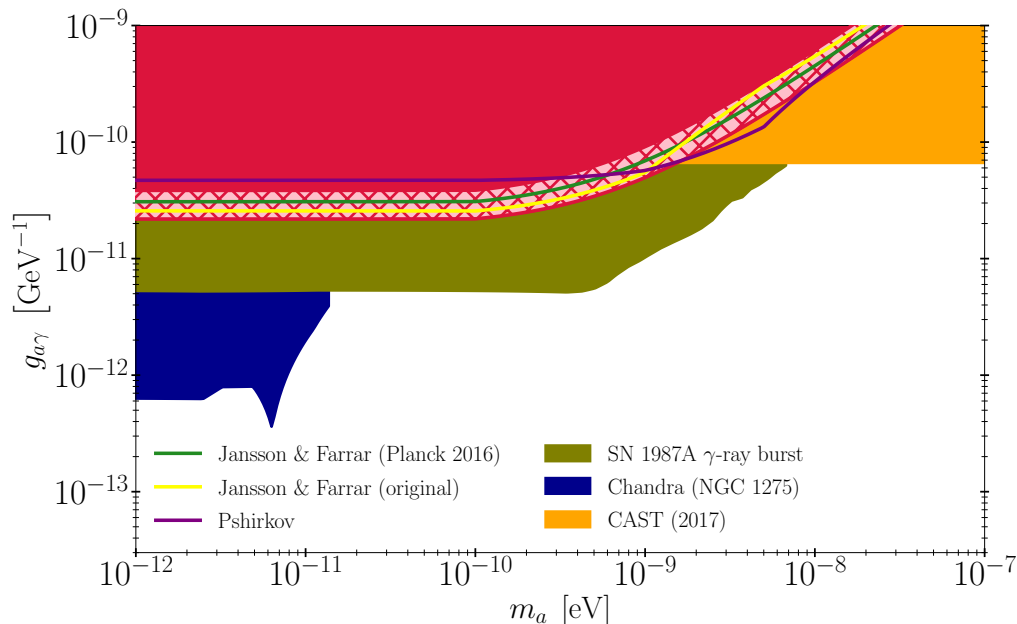


FIG. 9. As in Fig. 8. However, here we focus on the variation with respect to the magnetic field model. For definiteness, we choose the DSNALPB spectrum corresponding to $f_{\text{fail-CC}} = 20\%$ (see Tab. III). We confront the upper limits derived with different characterisations of the Milky Way’s magnetic field; ‘Jansson12a’ and ‘Jansson12c’ [85] (blue, green) and ‘Pshirkov’ [88] (purple). For comparison, the theoretical uncertainty due to the fraction of failed and successful CC SNe is shown as a light red band.

energy photons when experiencing the magnetic field of the Galaxy.

We presented a refined calculation of the ALPs flux from extragalactic SNe: we go beyond the simple approximation that the ALPs flux is independent on the SN mass progenitor by modeling the ALPs signal from different state-of-the-art SN models with progenitor masses between 8.8 and $70 M_{\odot}$. Moreover, we accounted for the possibility that not all CC SNe lead to successful explosions, by quantifying the fraction of failed CC SN explosions and building the corresponding model for the ALPs signal upon two simulations of failed CC SN explosions.

We explored four different scenarios, each of them characterized by a different fraction of failed CC SN explosions, allowing us to quantify the uncertainty due to failed CC SN explosions. The calculation of the ALPs flux from all past cosmic SNe accounts also for uncertainties related to the cosmic SN rate.

Using this new model for the diffuse supernova ALP background (DSNALPB) gamma-ray flux, we run a systematic analysis of 12 years of data collected by *Fermi*-LAT with the aim of setting robust upper limits on the ALPs parameter space. For the first time in the context of ALPs searches, we performed a template-based gamma-ray analysis to fully exploit the spatial features of the ALPs signal. The flux from the DSNALPB being peaked at about 50 MeV, we exploited the full LAT data sets by developing an optimized low-energy ($E \lesssim 200$ MeV) analysis. Besides, we optimized the interstellar emission (IE) models in a data-driven way and limit

the impact of the IE mis-modeling on the final limits – which, indeed, are only mildly affected by changing the IE model. We also selected the region of interest in order to be able to set statistically sound upper limit on the signal model.

Our final limits are a factor of a few better than the CAST bound (in the low mass region). However, they are still a factor of 8 above the SN1987A gamma-ray burst limit. It is nevertheless a nice confirmation, as they do not depend on a single event. More importantly, we quantified for the first time the width of the uncertainty band of the DSNALPB limit, which turns out to be less than a factor of 2 and dominated by the uncertainty on the fraction of failed CC SN explosions. Uncertainties on the IE model are sub-dominant, while those on the Galactic magnetic field remain an important source of systematic uncertainties for ALPs searches.

Although the numerical values of our limits change only by a modest amount compared to previous results, we believe that the present work offers a uniquely coherent and robust analysis of the DSNALPB signal with *Fermi*-LAT data.

ACKNOWLEDGMENTS

The work of P.C. is partially supported by the European Research Council under Grant No. 742104 and by the Swedish Research Council (VR) under grants 2018-03641 and 2019-02337. The work of P.C. and A.M. is par-

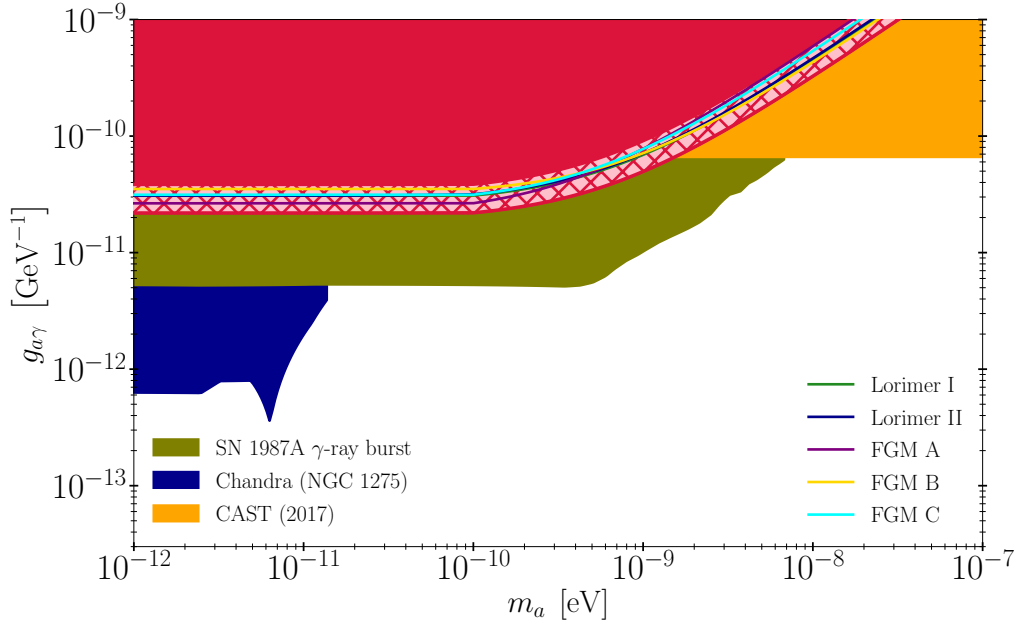


FIG. 10. As in Fig. 9 but here we focus on the dependence with respect to the background model. We compare the upper limits derived with our benchmark choice of IEM ‘Lorimer I’ (green) with four alternative interstellar emission models (c.f. Sec. IV B). Again, for comparison, the theoretical uncertainty due to the fraction of failed and successful CC SNe is shown as a light red band.

tially supported by the Italian Istituto Nazionale di Fisica Nucleare (INFN) through the “Theoretical Astroparticle Physics” project and by the research grant number 2017W4HA7S “NAT-NET: Neutrino and Astroparticle Theory Network” under the program PRIN 2017 funded by the Italian Ministero dell’Università e della Ricerca (MUR). The work of C.E. is supported by the “Agence Nationale de la Recherche”, grant n. ANR-19-CE31-0005-01 (PI: F. Calore). T.F. acknowledges support from the Polish National Science Center (NCN) under Grant

No. 2020/37/B/ST9/00691. Numerical computations of T.K. were carried out on Cray XC50 at CfCA, NAOJ and on Sakura and Raven at Max Planck Computing and Data Facility. The work of M.G. is partially supported by a grant provided by the Fulbright U.S. Scholar Program and by a grant from the Fundación Bancaria Ibercaja y Fundación CAI. M.G. thanks the Departamento de Física Teórica and the Centro de Astropartículas y Física de Altas Energías (CAPA) of the Universidad de Zaragoza for hospitality during the completion of this work.

-
- [1] C. Eckner, F. Calore, P. Carenza, M. Giannotti, J. Jaeckel, F. Sivo, and A. Mirizzi, in *Proceedings of 37th International Cosmic Ray Conference — PoS(ICRC2021)*, Vol. 395 (2021) p. 543.
 - [2] P. Agrawal *et al.*, (2021), arXiv:2102.12143 [hep-ph].
 - [3] G. G. Raffelt, *Stars as laboratories for fundamental physics: The astrophysics of neutrinos, axions, and other weakly interacting particles* (1996).
 - [4] G. G. Raffelt, *Lect. Notes Phys.* **741**, 51 (2008), arXiv:hep-ph/0611350.
 - [5] T. Fischer, S. Chakraborty, M. Giannotti, A. Mirizzi, A. Payez, and A. Ringwald, *Phys. Rev. D* **94**, 085012 (2016), arXiv:1605.08780 [astro-ph.HE].
 - [6] J. W. Brockway, E. D. Carlson, and G. G. Raffelt, *Phys. Lett. B* **383**, 439 (1996), arXiv:astro-ph/9605197.
 - [7] J. A. Grifols, E. Masso, and R. Toldra, *Phys. Rev. Lett.* **77**, 2372 (1996), arXiv:astro-ph/9606028.
 - [8] P. Carenza, T. Fischer, M. Giannotti, G. Guo, G. Martínez-Pinedo, and A. Mirizzi, *JCAP* **10**, 016 (2019), [Erratum: *JCAP* **05**, E01 (2020)], arXiv:1906.11844 [hep-ph].
 - [9] G. Lucente, P. Carenza, T. Fischer, M. Giannotti, and A. Mirizzi, *JCAP* **12**, 008 (2020), arXiv:2008.04918 [hep-ph].
 - [10] A. Payez, C. Evoli, T. Fischer, M. Giannotti, A. Mirizzi, and A. Ringwald, *JCAP* **02**, 006 (2015), arXiv:1410.3747 [astro-ph.HE].
 - [11] M. Meyer, M. Giannotti, A. Mirizzi, J. Conrad, and M. A. Sánchez-Conde, *Phys. Rev. Lett.* **118**, 011103 (2017), arXiv:1609.02350 [astro-ph.HE].
 - [12] M. Meyer and T. Petrushevska, *Phys. Rev. Lett.* **124**, 231101 (2020), [Erratum: *Phys. Rev. Lett.* **125**, 119901 (2020)], arXiv:2006.06722 [astro-ph.HE].
 - [13] M. Meyer and T. Petrushevska (Fermi-LAT), *PoS ICRC2021*, 510 (2021), arXiv:2108.02069 [astro-ph.HE].
 - [14] M. Crnogorčević, R. Caputo, M. Meyer, N. Omodei, and M. Gustafsson, (2021), arXiv:2109.05790 [astro-ph.HE].

- [15] G. G. Raffelt, J. Redondo, and N. Viaux Maira, *Phys. Rev. D* **84**, 103008 (2011), arXiv:1110.6397 [hep-ph].
- [16] F. Calore, P. Carenza, M. Giannotti, J. Jaeckel, and A. Mirizzi, *Phys. Rev. D* **102**, 123005 (2020), arXiv:2008.11741 [hep-ph].
- [17] J. R. Mattox *et al.*, *Astrophys. J.* **461**, 396 (1996).
- [18] M. Su, T. R. Slatyer, and D. P. Finkbeiner, *Astrophys. J.* **724**, 1044 (2010), arXiv:1005.5480 [astro-ph.HE].
- [19] M. Ackermann *et al.*, *Astrophys. J.* **761**, 91 (2012), arXiv:1205.6474 [astro-ph.CO].
- [20] M. Ackermann *et al.* (Fermi-LAT), *Astrophys. J.* **840**, 43 (2017), arXiv:1704.03910 [astro-ph.HE].
- [21] E. Storm, C. Weniger, and F. Calore, *JCAP* **08**, 022 (2017), arXiv:1705.04065 [astro-ph.HE].
- [22] M. Di Mauro, X. Hou, C. Eckner, G. Zaharijas, and E. Charles, *Phys. Rev. D* **99**, 123027 (2019), arXiv:1904.10977 [astro-ph.HE].
- [23] M. Di, *Phys. Rev. D* **103**, 063029 (2021), arXiv:2101.04694 [astro-ph.HE].
- [24] A. Mezzacappa and S. Bruenn, *Astrophys. J.* **405**, 669 (1993).
- [25] M. Liebendörfer, O. Messer, A. Mezzacappa, S. Bruenn, C. Cardall, *et al.*, *Astrophys. J. Suppl.* **150**, 263 (2004).
- [26] T. Fischer, *Astron. Astrophys.* **593**, A103 (2016).
- [27] T. Fischer, G. Guo, A. A. Dzhioev, G. Martínez-Pinedo, M.-R. Wu, A. Lohs, and Y.-Z. Qian, *Phys. Rev. C* **101**, 025804 (2020).
- [28] T. Kuroda, T. Fischer, T. Takiwaki, and K. Kotake, arXiv e-prints, arXiv:2109.01508 (2021), arXiv:2109.01508 [astro-ph.HE].
- [29] K. Kotake, T. Takiwaki, T. Fischer, K. Nakamura, and G. Martínez-Pinedo, *Astrophys. J.* **853**, 170 (2018).
- [30] J. M. Lattimer and F. Swesty, *Nucl. Phys. A* **535**, 331 (1991).
- [31] H. Shen, H. Toki, K. Oyamatsu, and K. Sumiyoshi, *Nucl. Phys. A* **637**, 435 (1998).
- [32] M. Hempel and J. Schaffner-Bielich, *Nucl. Phys. A* **837**, 210 (2010).
- [33] M. Hempel, T. Fischer, J. Schaffner-Bielich, and M. Liebendörfer, *Astrophys. J.* **748**, 70 (2012).
- [34] A. W. Steiner, M. Hempel, and T. Fischer, *Astrophys. J.* **774**, 17 (2013).
- [35] K. Nomoto, *Astrophys. J.* **322**, 206 (1987).
- [36] F. Kitaura, H.-T. Janka, and W. Hillebrandt, *Astron. Astrophys.* **450**, 345 (2006).
- [37] T. Fischer, S. Whitehouse, A. Mezzacappa, F.-K. Thielemann, and M. Liebendörfer, *Astron. Astrophys.* **517**, A80 (2010).
- [38] S. E. Woosley, A. Heger, and T. A. Weaver, *Rev. Mod. Phys.* **74**, 1015 (2002).
- [39] T. Baumgarte, S. Teukolsky, S. Shapiro, H. Janka, and W. Keil, *Astrophys. J.* **468**, 823 (1996).
- [40] K. Sumiyoshi, S. Yamada, H. Suzuki, and S. Chiba, *Phys. Rev. Lett.* **97**, 091101 (2006), arXiv:astro-ph/0608509 [astro-ph].
- [41] T. Fischer, S. C. Whitehouse, A. Mezzacappa, F.-K. Thielemann, and M. Liebendörfer, *Astron. Astrophys.* **499**, 1 (2009).
- [42] E. O'Connor and C. D. Ott, *Astrophys. J.* **730**, 70 (2011), arXiv:1010.5550 [astro-ph.HE].
- [43] T. Fischer, N.-U. F. Bastian, M.-R. Wu, P. Baklanov, E. Sorokina, S. Blinnikov, S. Typel, T. Klähn, and D. B. Blaschke, *Nat. Astron.* **2**, 980 (2018).
- [44] T. Fischer, arXiv e-prints, arXiv:2108.00196 (2021), arXiv:2108.00196 [astro-ph.HE].
- [45] K. Takahashi, H. Umeda, and T. Yoshida, *Astrophys. J.* **794**, 40 (2014), arXiv:1406.5305 [astro-ph.SR].
- [46] T. Kuroda, K. Kotake, T. Takiwaki, and F.-K. Thielemann, *Mon. Not. Roy. Astron. Soc.* **477**, L80 (2018), arXiv:1801.01293 [astro-ph.HE].
- [47] S. Shibagaki, T. Kuroda, K. Kotake, and T. Takiwaki, *Mon. Not. Roy. Astron. Soc.* **502**, 3066 (2021), arXiv:2010.03882 [astro-ph.HE].
- [48] G. Raffelt and L. Stodolsky, *Phys. Rev. D* **37**, 1237 (1988).
- [49] G. G. Raffelt, *Phys. Rev. D* **33**, 897 (1986).
- [50] J. F. Beacom, *Ann. Rev. Nucl. Part. Sci.* **60**, 439 (2010), arXiv:1004.3311 [astro-ph.HE].
- [51] N. Aghanim *et al.* (Planck), *Astron. Astrophys.* **641**, A6 (2020), arXiv:1807.06209 [astro-ph.CO].
- [52] A. M. Hopkins and J. F. Beacom, *Astrophys. J.* **651**, 142 (2006), arXiv:astro-ph/0601463.
- [53] S. Horiuchi, J. F. Beacom, C. S. Kochanek, J. L. Prieto, K. Z. Stanek, and T. A. Thompson, *Astrophys. J.* **738**, 154 (2011), arXiv:1102.1977 [astro-ph.CO].
- [54] G. J. Mathews, J. Hidaka, T. Kajino, and J. Suzuki, *Astrophys. J.* **790**, 115 (2014), arXiv:1405.0458 [astro-ph.CO].
- [55] I. K. Baldry and K. Glazebrook, *Astrophys. J.* **593**, 258 (2003), arXiv:astro-ph/0304423.
- [56] T. A. Gutcke and V. Springel, *Mon. Not. Roy. Astron. Soc.* **482**, 118 (2019), arXiv:1710.04222 [astro-ph.GA].
- [57] D. Kresse, T. Ertl, and H.-T. Janka, *Astrophys. J.* **909**, 169 (2021), arXiv:2010.04728 [astro-ph.HE].
- [58] K. Møller, A. M. Suliga, I. Tamborra, and P. B. Denton, *JCAP* **05**, 066 (2018), arXiv:1804.03157 [astro-ph.HE].
- [59] O. Pejcha and T. A. Thompson, *Astrophys. J.* **801**, 90 (2015), arXiv:1409.0540 [astro-ph.HE].
- [60] T. Ertl, H. T. Janka, S. E. Woosley, T. Sukhbold, and M. Ugliano, *Astrophys. J.* **818**, 124 (2016), arXiv:1503.07522 [astro-ph.SR].
- [61] C. A. Raithel, T. Sukhbold, and F. Özel, *Astrophys. J.* **856**, 35 (2018), arXiv:1712.00021 [astro-ph.HE].
- [62] T. Sukhbold, T. Ertl, S. E. Woosley, J. M. Brown, and H. T. Janka, *Astrophys. J.* **821**, 38 (2016), arXiv:1510.04643 [astro-ph.HE].
- [63] J. Hidaka, T. Kajino, and G. J. Mathews, *Astrophys. J.* **827**, 85 (2016).
- [64] S. M. Adams, C. S. Kochanek, J. R. Gerke, and K. Z. Stanek, *Mon. Not. Roy. Astron. Soc.* **469**, 1445 (2017), arXiv:1610.02402 [astro-ph.SR].
- [65] T. Fischer, M.-R. Wu, B. Wehmeyer, N.-U. F. Bastian, G. Martínez-Pinedo, and F.-K. Thielemann, *Astrophys. J.* **894**, 9 (2020), arXiv:2003.00972 [astro-ph.HE].
- [66] A. Lien, B. D. Fields, and J. F. Beacom, *Phys. Rev. D* **81**, 083001 (2010), arXiv:1001.3678 [astro-ph.CO].
- [67] R. Jansson and G. R. Farrar, *Astrophys. J.* **757**, 14 (2012), arXiv:1204.3662 [astro-ph.GA].
- [68] R. Adam *et al.* (Planck), *Astron. Astrophys.* **596**, A103 (2016), arXiv:1601.00546 [astro-ph.GA].
- [69] M. S. Pshirkov, P. G. Tinyakov, P. P. Kronberg, and K. J. Newton-McGee, *Astrophys. J.* **738**, 192 (2011), arXiv:1103.0814 [astro-ph.GA].
- [70] J. M. Cordes and T. J. W. Lazio, (2002), arXiv:astro-ph/0207156.
- [71] K. M. Górski, E. Hivon, A. J. Banday, B. D. Wandelt, F. K. Hansen, M. Reinecke, and M. Bartelmann, *ApJ*

- 622**, 759 (2005), arXiv:astro-ph/0409513 [astro-ph].
- [72] G. Cowan, K. Cranmer, E. Gross, and O. Vitells, *Eur. Phys. J. C* **71**, 1554 (2011), [Erratum: *Eur. Phys. J. C* **73**, 2501 (2013)], arXiv:1007.1727 [physics.data-an].
- [73] F. Acero *et al.* (Fermi-LAT), *Astrophys. J. Suppl.* **224**, 8 (2016), arXiv:1511.06778 [astro-ph.HE].
- [74] D. R. Lorimer *et al.*, *Mon. Not. Roy. Astron. Soc.* **372**, 777 (2006), arXiv:astro-ph/0607640.
- [75] M. Ackermann *et al.* (Fermi-LAT), *Astrophys. J.* **799**, 86 (2015), arXiv:1410.3696 [astro-ph.HE].
- [76] S. Abdollahi *et al.* (Fermi-LAT), *Astrophys. J. Suppl.* **247**, 33 (2020), arXiv:1902.10045 [astro-ph.HE].
- [77] J. Ballet, T. H. Burnett, S. W. Digel, and B. Lott (Fermi-LAT), (2020), arXiv:2005.11208 [astro-ph.HE].
- [78] L. Herold and D. Malyshev, *Astron. Astrophys.* **625**, A110 (2019), arXiv:1904.01454 [astro-ph.HE].
- [79] M. Wolleben, *Astrophys. J.* **664**, 349 (2007), arXiv:0704.0276 [astro-ph].
- [80] G. Johannesson and E. Orlando, in *International Cosmic Ray Conference*, International Cosmic Ray Conference, Vol. 33 (2013) p. 3106, arXiv:1307.0197 [astro-ph.IM].
- [81] O. Macias, S. Horiuchi, M. Kaplinghat, C. Gordon, R. M. Crocker, and D. M. Nataf, *JCAP* **09**, 042 (2019), arXiv:1901.03822 [astro-ph.HE].
- [82] H. Dembinski, P. Ongmongkolkul, C. Deil, D. M. Hurtado, M. Feickert, H. Schreiner, Andrew, C. Burr, F. Rost, A. Pearce, and et al., (2020), 10.5281/zenodo.4047970.
- [83] H.-S. Zechlin, S. Manconi, and F. Donato, *Phys. Rev. D* **98**, 083022 (2018), arXiv:1710.01506 [astro-ph.HE].
- [84] R. Jansson and G. R. Farrar, *Astrophys. J.* **757**, 14 (2012), arXiv:1204.3662 [astro-ph.GA].
- [85] R. Adam *et al.* (Planck), *Astron. Astrophys.* **596**, A103 (2016), arXiv:1601.00546 [astro-ph.GA].
- [86] V. Anastassopoulos *et al.* (CAST), *Nature Phys.* **13**, 584 (2017), arXiv:1705.02290 [hep-ex].
- [87] C. S. Reynolds, M. C. D. Marsh, H. R. Russell, A. C. Fabian, R. Smith, F. Tombesi, and S. Veilleux, (2019), 10.3847/1538-4357/ab6a0c, arXiv:1907.05475 [hep-ph].
- [88] M. S. Pshirkov, P. G. Tinyakov, P. P. Kronberg, and K. J. Newton-McGee, *Astrophys. J.* **738**, 192 (2011), arXiv:1103.0814 [astro-ph.GA].